International Journal of Heat and Mass Transfer 52 (2009) 181–192

Contents lists available at ScienceDirect

International Journal of Heat and Mass Transfer

journal homepage: www.elsevier.com/locate/ijhmt

Experimental and numerical study of transient natural convection due to mass transfer in inclined enclosures

D.Z. Jeng [a,1], C.S. Yang [b], C. Gau [a,*]

[a] Institute of Aeronautics and Astronautics and Center for Micro/Nano Science and Technology, National Cheng Kung University, Tainan 701, Taiwan
[b] Department of Computer Science and Information Engineering, Far East University, Tainan 710, Taiwan

ARTICLE INFO

Article history:
Received 22 January 2008
Received in revised form 3 June 2008
Available online 26 July 2008

Keywords:
Transient natural convection
Mass transfer in enclosure
Solutal convection in enclosure
Inclined enclosure

ABSTRACT

Both experiments and numerical work are performed to study transient natural convection flow and transport process due to mass transfer in the enclosures inclined at different angles. In the experiments, the enclosure is filled with aqueous solution containing $CuSO_4 + H_2SO_4$ where the flow structure can be visualized by both particle tracer and shadowgraph. Two opposed side walls of the enclosure are maintained at different concentrations which are made by passing current through the electrodes at the limiting condition. All the other side walls are made insulated and impermeable to the species transfer. Both the concentration distribution and its fluctuations are measured with non-intrusive optical method. During the experiments, the Rayleigh number ranges from 1.126×10^8 to 1.157×10^{11}, the angles of inclination from 30 to 90 degree and the aspects ratio of the enclosure from 0.6 to 1. Comparison between the data and prediction is made and discussed at various conditions.

1. Introduction

The study of natural convection in enclosures has wide applications in a number of diverse fields, for example, thermal insulations for building and solar collectors; cooling systems for nuclear reactors, convective processes in lakes; and the growth of crystals for semiconductor industry. The idealized problem of laminar convection in an enclosed rectangular cavity with differentially heated end walls has been extensively studied in various contexts. These investigations have, for the most part, been concerned with steady-state situation. Yet in many of the fields of application listed above, the convective flows may be in a transient or unsteady state in an enclosure. Recognizing this fact, some of the recent works in this field have focused on the nature of the flow in the transient regime and the manner in which this flow evolves into the final steady state.

Patterson and Imberger [1] (hereinafter referred to as PI) based on scale analysis have obtained six different flow regimes and the manners in which this flow evolved into final steady state. Of particular interest is the flow regime IV, V and VI, defined by PI, which involve existence of internal wave motions. The internal wave motions are due to tilting of the isotherms owing to a piling up of intruding flow at the opposite side of the cavity, which dies away when steady state is reached. Ivey [2] performed the experiments in flow regime IV and found the oscillations of flow. However, Ivey argued that the oscillation of flow was not the seiching type motion as suggested by PI, but due to the inertia of the flow entering the interior of the cavity from the sidewall boundary layers, which may lead to a form of internal hydraulic jump. The experimental results agree with the numerical simulation [3]. For a higher *Pr* number fluid convection, however, both oscillation and internal wave motion of flow was not observed. Flow pattern between the case of low *Pr* number fluid and the case of high *Pr* number fluid is significantly different. A series of numerical simulations based on one of the flow cases, which was in flow regime IV studied by Ivey [2], is performed [4]. It was claimed that most of the transient flow pattern could be qualitatively simulated. However, the counter rotation of core found in Ivey's experiments is attributed to the slightly thermal stratification occurred in the bulk fluid before starting the experiments.

A more detailed study on the transient natural convection flow in regime IV has been conducted both experimentally and numerically [5] which provides more information on the features and development of flow structure. The boundary layer instabilities which cause the oscillations of temperature in the intrusion and the presence of cavity-scale oscillations caused by the interaction of the intrusions with the opposing vertical boundary layer are identified and discussed. Schladow [6] analyzed numerically the oscillation motion of fluid and found the presence of both long-period and short-period oscillations. The temperature oscillations found by Ivey is actually attributed to the short-period oscillation produced by two distinct boundary layer instabilities. The long-period oscillation is actually the internal wave

* Corresponding author. Tel.: +886 6 2757575; fax: +886 6 2389940.
E-mail address: gauc@mail.ncku.edu.tw (C. Gau).
[1] Present address: Aeronautical Research Laboratory, Chung Shan Institute of Science and Technology, Taichung, Taiwan.

0017-9310/$ - see front matter © 2008 Elsevier Ltd. All rights reserved.
doi:10.1016/j.ijheatmasstransfer.2008.06.012

Nomenclature

Ar	aspect ratio, H/L
C	concentration of cupric ion
D	solutal diffusivity
g	gravitational acceleration or gram
Gr	Grashof number, $g\,\beta_s(C_a - C_c)H^3/\nu^2$
H	height of the enclosure
L	width of the enclosure
p	pressure
Ra	solutal Rayleigh number, $g\,\beta_s(C_a - C_c)H^3/\nu D$
Sc	Schmidt number
t	time
u	velocity in x-direction
v	velocity in y-direction
x	coordinate normal to the electrodes
y	coordinate parallel to the electrodes
z	coordinate normal to the core flow motion or both x and y axis

Greek symbols

β	volumetric coefficient of expansion due to dissolution
ρ	density
ν	kinematic viscosity
τ	dimensionless time

Subscripts

a	refer to anode
b	refer to bulk or core
c	refer to cathode
s	refer to solutal

Superscripts

–	refer to the dimensionless quantity

motion as described by PI. It appears that natural convection of the transient flow structure is so complex that it deserves more research attention.

Moreover, owing to the occurrence of natural convection in an inclined layer is rather common since rarely is the earth's surface aligned with geo-potential lines, increasing attention has been paid to the problem of natural convection in inclined enclosures [7–17], but there is still a serious lack of information regarding the transient process of natural convection in an inclined enclosure. In addition, most of the prior studies on cavity convection were in side-heated enclosures. No information is found for natural convection induced by mass transfer. In addition, the experiment with side-heated enclosures has an inherent difficulty that can not simulate a perfect insulation wall and completely eliminate the heat conduction or the heat loss along the wall. This can significantly affect the flow and transport process inside the enclosure. To avoid these difficulties, the current study uses an electrochemical system which can induce natural convection by solutal diffusion.

The electrochemical system selected employs a diffusion-controlled electrolytic reaction. When an externally applied potential across the two electrodes is at such a critical value that the current passing through the electrolyte reaches limiting condition, an iso-concentration condition on the cupric electrode can be made. The concentration on the anode surface is twice the concentration of the bulk fluid, while the concentration on the cathode is zero. Since both the energy equation and the species diffusion equation are analogous, using appropriate heat-mass transfer analogy, the results obtained from current solutal convection experiment can be used to simulate the corresponding thermal convection experiment. The electrochemical system has the advantages of providing a side wall with no side wall conduction and radiation which can have a better control of boundary condition. In addition, the electrolyte usually is a very high Schmidt number fluid which allows simulation of high Pr and tl number fluid convection. Goldstein et al. [17,18] employed the same system to study high Rayleigh number solutal convection mass transfer in the enclosures and obtained correlation of mass transfer Sherwood number in terms of Rayleigh number. The same system had also been used to study thermal–solutal convection in the enclosure [19].

The electrolyte used in the current system is an aqueous solution containing 0.05 M $CuSO_4$ and 1.5 M H_2SO_4. The present system has a Schmidt number of 2772 and Rayleigh number of 3.53×10^9 to 2.11×10^9, which leads to a condition that $Ra > Sc^2$. Therefore, the flow condition corresponds to the flow regime III as described by PI.

In the present study, a joint experimental and numerical work is performed which attempts to gain detailed understanding of the transient process of the flow structure and mass transfer in the inclined, low aspect ratio enclosures. The Simple algorithm [20] is employed to calculate the solutal convection under the experimental conditions. Comparison between the prediction and data is made. The agreement between the prediction and the data suggests that the current electrochemical system can be used to study transient development of natural convection in an inclined enclosure. The effect of inclination and aspect ratio of the enclosure on the development of flow structure and the transport process is presented and discussed.

2. Experimental apparatus and procedures

The rectangular test cell is made of 20-mm-thick plexiglass and has inside dimensions of 25 mm in height, 25 mm in width and 48 mm in depth. Both the vertical side walls of the enclosure are made of 12-mm-thick copper plate and serve as both the electrodes and the heat sources/sinks. Two identically shaped rectangular heat exchangers are each bolted with and used for controlling the temperature of the copper plate, as shown in Fig. 1. The temperature of each of the copper plate is maintained uniform and close to the room temperature by circulating room temperature water through the heat exchanger. An air gap is made outside and used for insulation to avoid possible heat transfer to or

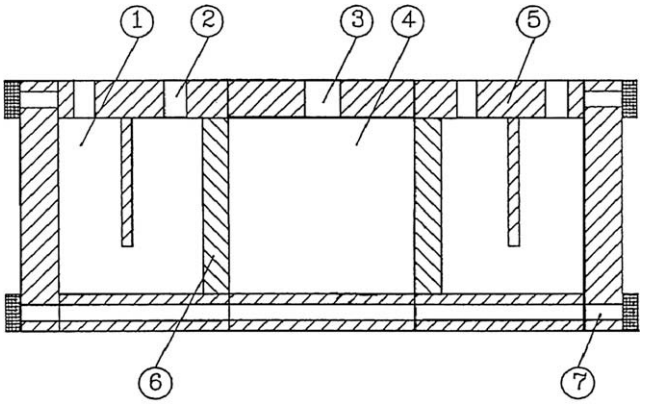

Fig. 1. Schematic diagram of the enclosure: (1) heat exchanger, (2) circulation water inlet/outlet, (3) filling hole, (4) test cell, (5) Plexiglass plate, (6) copper plate and (7) thread fastener.

from the outside. The top plate of the test cell can be moved downward so that the aspect ratio of the enclosure can be varied from 1 to 0.6.

To initiate electrolysis between the two electrodes, a DC power supply is used to provide the desired current. A digital multimeter and a recorder were connected in parallel to the electronic circuit to measure the temporal variation of the potential and the current.

A 25 mW He–Ne laser is employed as a light source for the measurement of the concentration in the solution. The light beam passing through the solution is partially absorbed. The change of light intensity, which according to Lambert–Beer's law is proportional to the magnitude of the local concentration of the solution, is measured with a power meter. Both the laser light source and the power detector are placed on the same traversing system that the light beam can be moved readily to the desired location for concentration measurements. The power meter has been calibrated and has a measurement accuracy of 1%. To measure concentration oscillation in the flow, the same apparatus is used. To avoid the noise generation, however, a reference beam which is split from the original laser light is made. The reference beam is directed to pass through a similar test cell with no convection occurring inside. A differential amplifier is used to measure the signal difference between the reference and the objective beam, which is a result of concentration oscillation in the test cell. With this apparatus, the noise signal from laser beam can be reduced significantly.

For flow visualization, the polystyrene powder with diameter of 6 μm is used as a tracer to delineate and visualize the fluid motion. The laser beam from the 25 mW He–Ne laser is made into a sheet of light by passing through a small diameter of cylindrical rod made of glass. This sheet of light is made parallel to the direction of the core flow motion and is used to visualize the entire flow motion in a plane perpendicular to the z-axis. During flow visualization, the sheet of light is moved back and forth in the z-axis to ensure that the flow structure at different z-axis is very similar and the flow in the test cell can be considered as two dimensional. As an alternative, the shadowgraph technique is used to visualize the density interface and the solutal plume phenomenon. At this time, the laser beam is expanded with a spatial filter and is then collimated with a large diameter of plane convex lens. The collimated light passing through the region having large variation of refractive index is deflected, and causes shadow on the screen. The solutal plume and layer interface in the flow that has relatively large variation of refractive index can be clearly observed. A Nikon FM2 camera with a 55-mm micro-lens is used for photographing.

Since the electrode surfaces can become roughened due to a long period of deposition of cupric ion, they can be readily detached from the test cell for polish and cleaning. After the surface is cleaned, the prepared solution is carefully poured into the enclosure. Precautions are made to prevent the air bubble trapped inside. The entire test cell is placed on a platform which can be rotated and adjusted to ensure the test cell inclined at desired angles.

Before the experiment, the copper sulfate solution having concentration from 0.05 M is prepared. The amount of the distilled water is measured with graduated cylinder. The copper sulfate powder is carefully weighted on a precision electronic balance, which has an accuracy of ±0.001 g, and is then mixed with a given amount of distilled water to reach the desired concentration. Finally, the H_2SO_4 solution is added into the mixed solution as a supporting electrolyte. The concentration of H_2SO_4 is 1.5 M. The thermal, chemical and transport properties of the solution are well documented in Wilke et al. [21]. Therefore, the concentration of the solution prepared has a maximum uncertainty of 0.5%. Follow the error analysis developed in [22], the concentration measured has a maximum uncertainty of 2.5%.

The electrolysis in the solution is initiated by switching on the DC power supply. To maintain the current density on the limiting current condition, the value of limiting current has to be measured before the experiment. The limiting current condition is determined by the potentiostatic-current method. The cell voltage is set with manual control in a stepwise manner, and the corresponding current is obtained and recorded. The procedure is repeated until the potential-current plateau is attained. More details on the limiting current measurement can be found in [21,23].

3. Numerical calculation

3.1. Mathematical formulation

The experimental test cell is modeled with a two-dimensional rectangular enclosure, as shown in Fig. 2, having width L and height H and containing $CuSO_4 + H_2SO_4$ electrolyte solution. Both the top and the bottom walls are well insulated. The solution is assumed to be incompressible and Boussinesq-type. Initially, the working fluid is stagnant and at a uniform concentration C_b. As time $t > 0$, the concentration on one of the side walls, i.e. the cathode, is immediately reduced to 0, and that on the opposite wall, i.e. the anode, is raised to $2C_b$ and maintained at that value thereafter. Therefore, buoyancy-induced flow associated with mass transfer process can be initiated which develops with time. The physical process can be described by a set of differential equations. For simplicity, before the numerical calculation the governing equations are non-dimensionalized with the following dimensionless parameters:

$$\bar{x} = x/H, \quad \bar{y} = y/H, \quad \tau = t/(H^2/D),$$
$$\bar{u} = u/(D/H), \quad \bar{v} = v/(D/H), \quad \bar{p} = p/(\rho D^2/H^2)$$
$$\overline{C} = \tfrac{(C - C_b)}{C_b}, \quad Ar = H/L, \quad Sc = v/D,$$
$$Ra = \beta g 2C_b H^3/(vD)$$

Therefore, the non-dimensionalized equations can be written as follows [24]:

$$\frac{\partial \bar{u}}{\partial \bar{x}} + \frac{\partial \bar{v}}{\partial \bar{y}} = 0 \tag{1}$$

$$\frac{\partial \bar{u}}{\partial \tau} + \bar{u}\frac{\partial \bar{u}}{\partial \bar{x}} + \bar{v}\frac{\partial \bar{u}}{\partial \bar{y}} = -\frac{\partial \bar{p}}{\partial \bar{x}} + Sc\left(\frac{\partial^2 \bar{u}}{\partial \bar{x}^2} + \frac{\partial^2 \bar{u}}{\partial \bar{y}^2}\right) + RaSc\overline{C}\cos\phi \tag{2}$$

$$\frac{\partial \bar{v}}{\partial \tau} + \bar{u}\frac{\partial \bar{v}}{\partial \bar{x}} + \bar{v}\frac{\partial \bar{v}}{\partial \bar{y}} = -\frac{\partial \bar{p}}{\partial \bar{y}} + Sc\left(\frac{\partial^2 \bar{v}}{\partial \bar{x}^2} + \frac{\partial^2 \bar{v}}{\partial \bar{y}^2}\right) + RaSc\overline{C}\sin\phi \tag{3}$$

$$\frac{\partial \overline{C}}{\partial \tau} + \bar{u}\frac{\partial \overline{C}}{\partial \bar{x}} + \bar{v}\frac{\partial \overline{C}}{\partial \bar{y}} = \left(\frac{\partial^2 \overline{C}}{\partial \bar{x}^2} + \frac{\partial^2 \overline{C}}{\partial \bar{y}^2}\right) \tag{4}$$

with the initial and boundary conditions:

$$\tau = 0: \quad \bar{u} = \bar{v} = 0, \quad \overline{C} = 0$$
$$\tau > 0: \quad \bar{y} = 0, \quad \bar{u} = \bar{v} = 0, \quad \tfrac{\partial \overline{C}}{\partial \bar{y}} = 0$$
$$\bar{y} = 1, \quad \bar{u} = \bar{v} = 0, \quad \tfrac{\partial \overline{C}}{\partial \bar{y}} = 0$$
$$\bar{x} = 0: \quad \bar{u} = \bar{v} = 0, \quad \overline{C} = -1$$
$$\bar{x} = \tfrac{1}{Ar}, \quad \bar{u} = \bar{v} = 0, \quad \overline{C} = 1$$

3.2. Numerical procedure

The governing equations are discretized using the control volume approach of Patankar [20]. In addition, the power law formulation is employed to determine the combined advective and diffusive fluxes across the boundaries of each control volume. The unsteady term is treated with backward difference. The buoy-

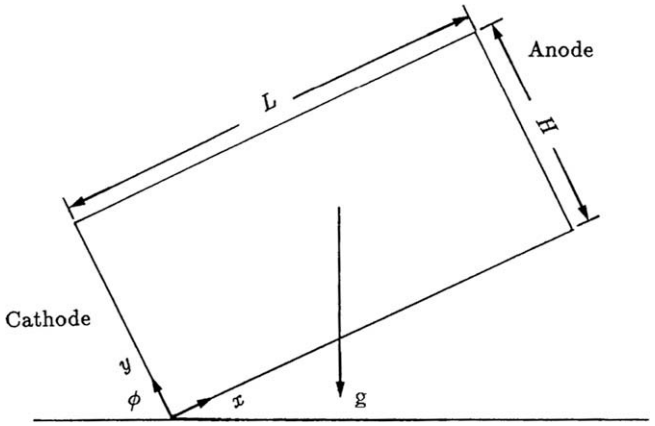

Fig. 2. Calculation model for a two-dimensional rectangular enclosure.

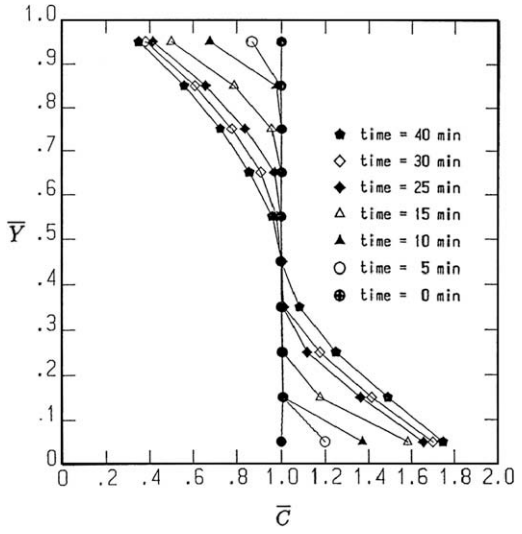

Fig. 3. Variations of vertical concentration distribution with times at $\bar{x} = 0.5$ for $Ra = 3.53 \times 10^9$.

ancy forces in the x and y-momentum equations are treated as source terms. The conventional stagger grid system used originally in the SIMPLE scheme is adopted. The discretized equations are solved iteratively with the line-by-line procedure of tri-diagonal matrix algorithm. To account for the drastic variations of the flow and concentration distribution during the initial period, a non-uniform time step is used. Depending on the Rayleigh number the $\Delta\tau$ in the beginning is set in a range from 1.74×10^{-7} to 1.74×10^{-6}, which corresponds to a real time from 0.031 to 0.31 s during the experiments.

Since the solutal boundary layer is confined in an extremely thin region along the wall, it is necessary to use a mesh that has relatively concentrated grids in the boundary layer and coarse grid in the interior. The mesh used here is such that the first grid near the vertical wall has one-thousandth of the cavity width and the following grid expands at a rate of 10% until that the solutal boundary layer edge is reached. From PI, the solutal boundary layer thickness is given by $\delta_s \sim H/Ra^{1/4}$. The minimum value of δ_s for the current experimental conditions is 0.1 mm, which has a non-dimensional thickness of 0.0041. To select a mesh width of 0.0005 of the cavity width for the first grid, one could have a total of six grid points in the solutal boundary layer. This results in a grid system of 100×100 points in the entire enclosure. Grid independence has also been checked and confirmed by using more grid points for calculations. Before the numerical simulation, the modified numerical code was verified [24] by comparing with a benchmark solution for natural convection of air in a square enclosure from De Vahl Davis [25] and others [26].

4. Results and discussion

4.1. $\phi = 90°$, $Ar = 1$

Before flow visualization was made, the vertical concentration distribution at the central location of the enclosure was measured at different times and is as shown in Fig. 3. Note that the concentration in the top of the enclosure decreases while that of the bottom increases over time. The vertical concentration distribution at different locations was also measured and found to be almost the same. It appears that fluid in both the top and bottom regions are concentrationally stratified. These stratified layers grow with time, which eventually combines together and form an entirely stratified core.

The results from the concentration measurements suggest that formation of the stratified layer is due to the lighter solutal boundary layer flow accumulating along the upper horizontal wall, while the heavier one accumulating along the lower horizontal plate. It is this accumulation that leads to the growth of the stratified layer. Therefore, the layer growth process is very similar to the filling box concept described in the reference [27], which can be readily modeled mathematically.

Flow visualization for the transient development of the flow over a 35-min duration, is shown in Fig. 4(a–i). Note that when electrolysis is initiated, the solutal boundary layers gradually form near both electrodes; the lighter fluid rises along the cathode wall, as shown in Fig. 4(a), while the heavier fluid descends along the anode wall. Note a very strong upward flow near the cathode (anode) 25–45 s after electrolysis has been initiated, and the whole flow embodies a single clockwise cell. Since the Schmidt number in this system is very high, the momentum boundary layer thickness is significantly higher than that of the solutal layer. According to PI, the momentum boundary layer thickness, δ, which is proportional to $\delta_s\ Sc^{1/2}$, is 5.16 mm in the current system, while the solutal boundary layer thickness, δ_s, which is proportional to $H/Ra^{1/4}$, is 0.116 mm. Therefore, most of the vertical upward or downward flow observed in Fig. 4(a) is actually the momentum boundary layer.

An examination of Fig. 4(a) reveals that once the left hand vertical boundary layer flow reaches the top wall, the flow rebounds slightly in its horizontal movement across to the opposite wall. Note also the existence of two expansion zones: one near the upper wall at $x/H = 0.133$ and the other near the lower wall at $x/H = 0.886$; phenomena which were also found in the experimental observations of [2,5,27], and in the numerical predications [4]. Ivey attributes these phenomena to the presence of an internal hydraulic jump, occurring when the internal Froude number ($Fr \sim Ra_t^{1/8}/Pr1/2$) of the intrusion flow is greater than unity. In the current condition, however, the internal Froude number of the intrusion is 0.3 which is less than unity. In addition, Ivey suggests that the internal hydraulic jump was the mechanism to cause the temperature fluctuations in the intrusion. However, the concentration oscillation measurements shown in the later figures indicate no oscillation of concentration in the intrusion. It appears that the appearance of the sudden expansion zone is attributed to the intrusion that is forced to flow under (over) undisplaced, relatively heavier (lighter) fluid on the top (bottom) of the cavity as explained by others [4].

At $t = 65$ s, note that the outer upward (downward) viscous layer flow severely rebounds away from the horizontal wall and moves downwards (upward), forming a secondary cell outside of

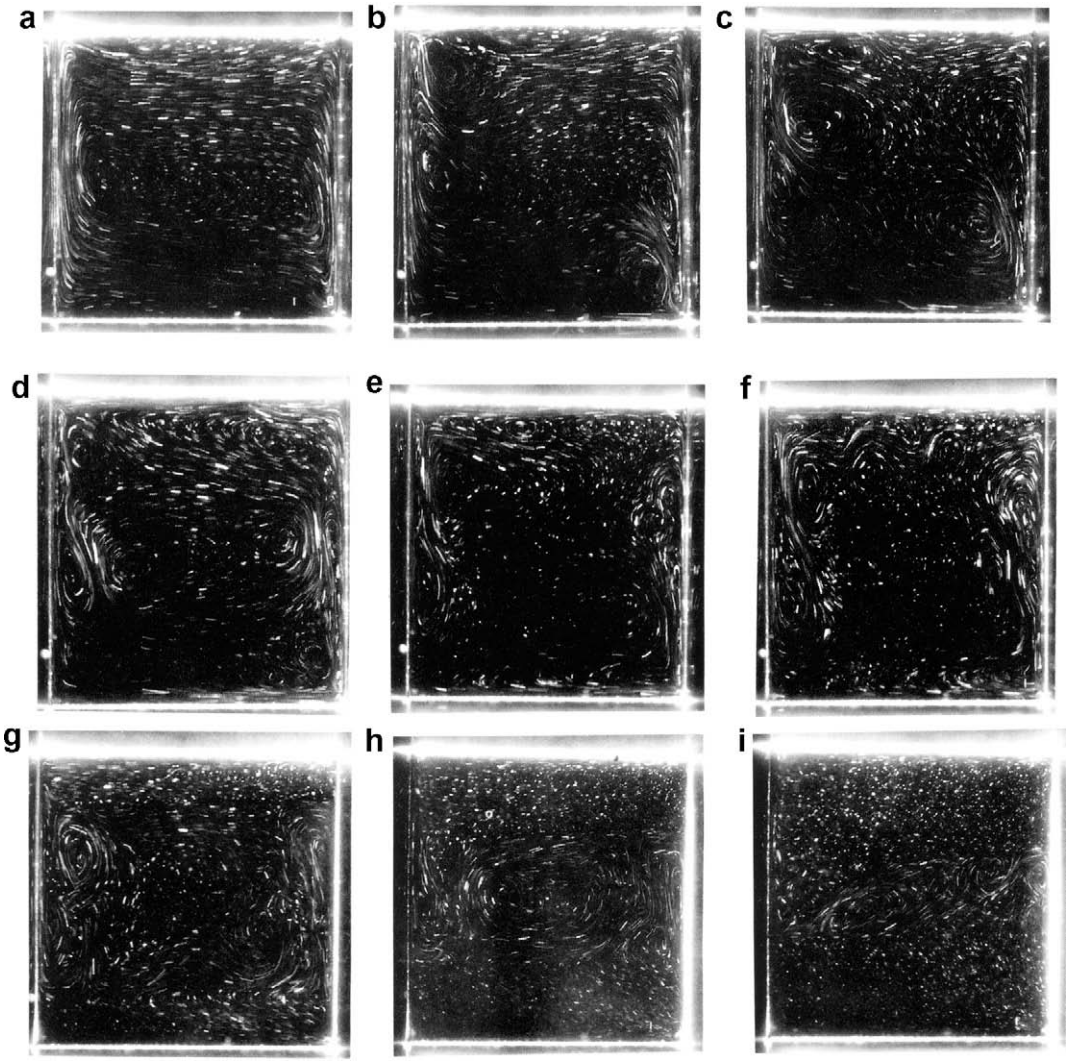

Fig. 4. Flow pattern for pure solutal convection with $Ra = 3.53 \times 10^9$, $Ar = 1$ for (a) $t = 45$ s, (b) $t = 65$ s, (c) $t = 115$ s, (d) $t = 145$ s, (e) $t = 225$ s, (f) $t = 375$ s, (g) $t = 700$ s, (h) $t = 1360$ s and (i) $t = 2060$ s (exposure time = 20 s).

the outer viscous layer as shown in Fig. 4(b). The downward (upward) movement of rebound flow near the cathode (anode) is attributed to the outer viscous flow that entrains and carries the heavier (lighter) horizontal intrusion in the bottom (top) wall to the top (bottom). Therefore, the secondary cells only appear after the heavier (lighter) components of the first intrusion flows are entrained and carried to the top (bottom) wall. Such secondary cells are also found in the thermal experiments of Ivey for $Ra = 3.8 \times 10^8$, $Pr = 78$ and Worster and Leitch [27] for $Ra = 6 \times 10^8$, $Pr = 16$, for a high Pr and tl number of fluid. At lower Pr and tl numbers, however, both numerical predictions and experimental results do not indicate formation of secondary cells. It appears that the formation of secondary cells is related to the Pr and tl number of fluid. For a lower Pr and tl number, the outer viscous layer has almost the same thickness as the inner thermal layer that the rebound of the vertical heated (cooled) flow from the horizontal wall may be so insignificant and the formation of secondary cells is not possible.

However, the lighter (heavier) solutal boundary layer flow does not rebound, but it turns and moves horizontally along the top (bottom) wall. It appears that the original, undisplaced fluid in the upper (lower) wall is pushed toward right (left) by the lighter (heavier) intrusion, as shown in Fig. 4(b–d), until it is entrained by the opposite downward (upward) viscous boundary layer flow. In addition to the secondary cell, the rebound of the outer viscous flow can gradually induce a counter clockwise vortex in the emerging region, i.e., in both the upper left and the lower right hand corner. The rebound of vertical viscous layer and the vortex induced near the corners are also observed in the thermal experiments [2] at a higher Pr. At a lower Pr, however, similar kind of vortices in the corners are not observed.

Note that the two original counter clockwise cells (above the secondary cell in the top-left hand corner and under the secondary cell in the bottom-right hand corner of the enclosure) gradually enlarges, which combine together and form a single counter clockwise circulation cell in the core, as shown in Fig. 4(c and d). A similar counter clockwise rotation of flow was also found in a heat transfer system of Ivey (1984), although a detailed explanation of the mechanism causing this rotation was not reported. Later, a numerical computation on a comparable system is performed [4] and found that this particular counter clockwise rotation of flow in the core only occurred when the cavity fluid was slightly thermally stratified at the beginning of the experiment. Interestingly enough, even though the current experiments were carefully performed and repeated in order to avoid any initial thermal or concentration stratification of the test cell, similar counter clockwise rotation of flow to that mentioned above was still found. It would therefore appear that the counter clockwise rotation of flow is not

due to initial stratification of fluid as reported in the literature, but rather as a result of the rotations of the two vortices near the cathode and anode plates. In general, however, the counter clockwise rotation in the core is not observed in the work at a low *Pr* due to the fact that the two vortices in the corners are not induced. Note in Fig. 4(d) that a new vortex has been generated. This vortex gradually enlarges at the corner of the cathode and the upper plate wall, while the old counter clockwise circulation cell in the core loses its momentum and disappears, as shown in Fig. 4(e). After 375 s (Fig. 4(f)), the wave-like flow structure appears directly under the upper plate. Similar phenomena can also be found in the literature of Ivey [2], who attributes this wave-like structure to the presence of the same internal hydraulic jump that also causes the temperature fluctuations. In the current experiments, however, a hydraulic jump does not occur for reasons already being explained. It may just be that the mechanisms responsible for this structure in both the current system and that of Ivey are different, and there is not enough information to clearly explain their behavior.

In general, the counter clockwise circulation cell exists as long as there is movement of flow in the core region. As this flow gradually reduces, the cavity fluid becomes increasingly stratified. This is due to the fact that most of the horizontal intrusion emerging from the solutal boundary layer accumulates along the horizontal wall and forms a thin layer near the top and the bottom walls. These layers are almost stagnant and concentrationally stratified, as shown in the concentration measurements in Fig. 3, which grows thicker with time, as shown in Fig. 4(g). The growth of the stratified layers makes the rotation of the flow in the core expelled into the central region. After 1360 s (Fig. 4(h)), the secondary cells near the cathode or the anode plate are still present, and numerous counter clockwise cells (in Fig. 4(g)) have merged, forming a large counter clockwise cell in the core. The circulation flow structure in the core gradually loses the momentum as shown in Fig. 4(i), until that both the top and the bottom layer combine and the entire bulk fluid becomes stagnant. In the present experiment, the time period for the combination of the stagnant layers is approximately 1 h.

Fig. 5(a–e) illustrate a series of numerically simulated streamlines and iso-concentration lines that follow the development of flow with time. An examination of Fig. 5(a) reveals that in additional to a large circulation cell, a pair of secondary cells which is circulated in the same direction as the large one in the outside occurs near both the electrodes due to the rebounds of the vertical viscous layers outside the solutal boundary layer flow.

Note that the flow structure at this time is very similar to that observed in the experiment. The upwardly moving fluid can push the secondary cell near the cathode upwards, while the fluid moving downwards pushes that near the anode downwards. The resulting flow structure is shown in Fig. 5(b). As seen in the constant-concentration-line diagrams of Fig. 5(c–e), the solutal intrusion flow moves forward along both the top and the bottom plates, eventually forming stratified layers in these regions once it reaches the opposite walls. Note that the fluid in this region moves very slowly along in the horizontal direction, enlarging with time and expelling the rotation of flow in the core. Moreover, note that the continuous enlargement process of the concentration stratification regions due to the accumulation of solutal boundary layer flow, is very similar to those observed in the experiments. It is noted again that the solutal gradient near the top or bottom insulated wall in Fig. 5(a–e) show very large gradient, suggesting mass transfer to the wall. In fact, the solutal gradient near the insulated is actually zero which could not be clearly observed in these figures due to very large concentration variation near the walls.

There are, however, a number of differences between the calculated and the experimental results. One such result that is not found in our prediction nor in the references [4,5], is the fact that

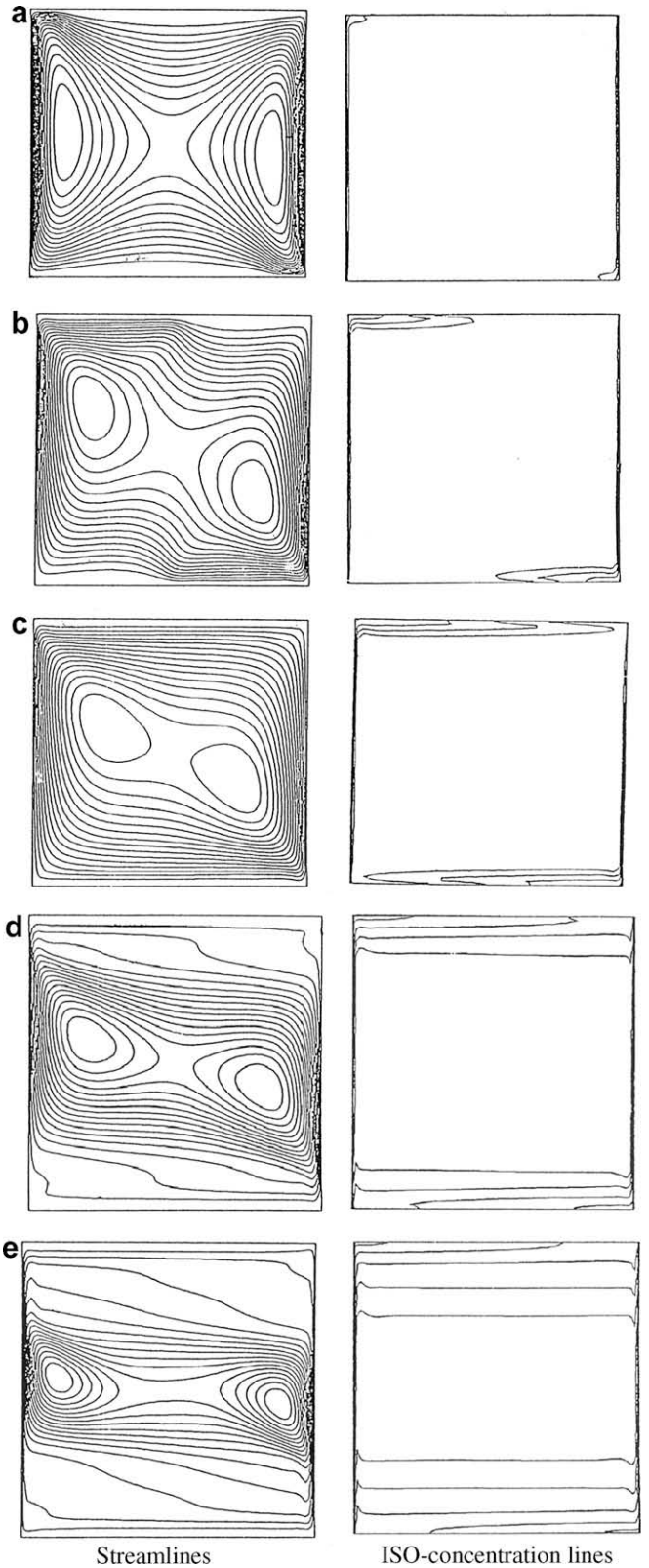

Fig. 5. Numerical simulation of streamline and iso-concentration contours at different times: (a) t = 100 s, (b) t = 200 s, (c) t = 300 s, (d) t = 500 s and (e) t = 1000 s.

a pair of counter clockwise eddies at both the upper-left hand corner of the cathode and the lower-left hand corner of the anode combine to form a counter clockwise rotating cell in the core region. The above-mentioned authors consider that the temperature stratification in the initial state is the major cause responsible for

generation of this counter clockwise rotating cell. Ivey [2] mentioned that such a counter clockwise rotation of the cell would be generated only at the initial stage of a transient process; a statement in direct contrast to what we observed experimentally, namely the counter clockwise cell is continuously generated due to the strong rotation of the two secondary cells near the cathode and anode plates and that it continues to exist until the core region becomes so narrow that it losses its movement completely and disappears. The fact that the numerical scheme fail to simulate the above phenomena is still not clear at present times. Even with a much refined grid and smaller time intervals, the simulation did not improve very much.

For $\phi = 90^\circ$ and $Ar = 0.6$, the flow structures are very similar to the ones for $Ar = 1$. However, when the aspect ratio decreases, the Ra correspondingly decreases, becoming 7.62×10^8 in this instance. Owing to the decrease in the aspect ratio and the distance between the two counter clockwise eddies in both the corners is relatively larger, so that the two eddies are unable to combine and form a large counter clockwise eddy, but generate a clockwise cell in the core instead. This result is the only difference from that obtained for $Ar = 1$. The solutal boundary layer flow can also intrude and accumulate along both the top and the wall, and form the stratified layer. The stratified layers can grow and push downward (upward) both the secondary cell and counter clockwise eddy near the cathode (anode). Moreover, these eddies gradually expand at the same time as the clockwise rotating cell in the core shrinks. At later time when the core becomes so narrow, the counter clockwise rotating eddy can split into a number of small eddies. Finally, the two stratified layers combine together and form a stratified core.

4.2. $\phi = 60^\circ$, $Ar = 0.6$

Fig. 6(a–g) illustrate a series of experimental results and numerical predictions over a number of time steps for a flow structure with $Ra = 7.62 \times 10^8$. The observed flow structure together with simulated flow field and concentration distribution diagrams are compared and discussed at every time step. Since the variation of flow structure with time is very slow, it can be expected that the streak line pattern in the photograph is very similar to the stream line results.

The numerically calculated flow field at $t = 90$ s (see the streamline diagram of Fig. 6(a)) indicated that two secondary cells form separately, one in the upper-left hand corner near the cathode and the other in the lower-right hand corner near the anode. Meanwhile, the intrusion flow of the concentration layer has just passed each corner in its forward movement along both the top and bottom walls (see the concentration contour diagram of Fig. 6(a)). At $t = 6$ min as shown in Fig. 6(b), the two secondary cells in the corners have merged and formed a large clockwise cell. These predictions are generally in agreement with the experimental observations, except that two weak individual cells can still be observed inside the large cell in the experiments. The large clockwise cell in this instance, forms in a completely different manner from that mentioned previously ($\phi = 90^\circ$, $Ar = 0.6$). In this case, the heavier (higher) intrusion flow fluid at the bottom (top) moving from the anode (cathode) is carried to the top (bottom) plate by the viscous boundary layer flow and instead of immediately rebounding downwards (upwards) after hitting this surface, it continues forward along the upper (bottom) plate for a distance, curving back down (up) to form a clockwise cell. The flow structure in this initial stage is similar to that reported by Patterson and Armfield [5] in a side-heated enclosure filled with water for $Ra = 3.26 \times 10^8$ and $Ar = 1$ at $\phi = 90^\circ$. In the current system, however, a concentration stratified region in both the upper and the lower corner of the enclosure can be formed, which becomes thicker with times and maintains stagnant. This causes the upper (lower) intrusion that enters the stratified layer deflected downwards (upwards) at an earlier stage and results in the separation of top cells from the wall. The prediction clearly indicates the appearance of two secondary cells and the downward (upward) deflection of the upper (lower) intrusion, as shown in Fig. 6(c), which agrees completely with the experimental observations.

At later time when the stratified region become thicker, it makes the two secondary cells in the core to shrink, as shown in both the prediction and the observed data in Fig. 6(d and e). At this stage, the core may have enough momentum for initiation of small eddies and vortices which are indicated in the predictions. However, it is very difficult to observe these small eddies in the flow visualization photograph. Finally, as the stratified layer become so thick that it may combine together and make the secondary cell to split into a number of small eddies as shown in Fig. 6(f). The occurrence of a number of small eddies for $\phi = 90^\circ$ was found in the center of the core before combination of the stratified layers. Once stratified layers combined together, however, they can completely suppress the cell motion in the core.

Generally, the experimental results compare favorably with predictions. One exception occurred at $t = 6$ min, where a slightly unsymmetric flow was observed in the photograph. The strength of the two clockwise cells seems to be greater than the predictions. This is no doubt, due to flow image overlap caused by the relatively long (30 s) exposure time that is chosen in order to obtain a discernible experimental flow path-line diagram. Even though a fast exposure would give cell sizes that more closely resemble the predictions, they are unfortunately, not distinct.

By observing the flow diagram more carefully, one finds that the size of the two clockwise eddies in the core does indeed match that of the calculated results. Another exception occurred at $t = 16$ min, where it is not obvious that the same small counter clockwise eddies and the weak clockwise eddies in the core exist in both the experimental results and the predictions.

Note again the split of the intrusion flow. The lighter stream of the solutal boundary layer moves along the upper plate and forms a solutal stratified layer in the top. The heavier stream is deflected from the upper plate, passes around the solutal stratified region and arrives at the anode to form a split region between the two streams, as shown in Fig. 6(c), which enlarges with time. As time increases, the split region moves back towards the emergent corner, as shown in Fig. 6(d), has penetrated sufficiently far to influence the divergent flow structure at that location. Similar situation occurs for the bottom intrusion flow from the anode to the cathode. The similar phenomenon was observed by Patterson and Armfield [5] in a side-heated enclosure with $\phi = 90^\circ$. They considered that such a mechanism is related to the generation of internal wave. In the past, the occurrence of internal wave was found in a side-heated enclosure in flow regime IV with $\phi = 90^\circ$. PI attributed the cause to a pile-up phenomenon which results when the intrusion flow from either the heated or the cooled plate arrives at their respective opposite walls. In the current experiments, the same pile-up phenomenon of the intrusion flow is observed. However, the current flow type belongs to the flow regime III, as defined by PI, where oscillation of the entire flow can not be generated. It appears that the inclination of the enclosure can make the oscillation of the entire flow to occur. This will be demonstrated in the later section for calculation of mass transfer oscillations.

As the split region was enlarged, the turn around movement of the forward moving fluid is more pronounced near the eddy in the left hand corner, which causes both the clockwise eddy in the core and the counter clockwise eddy near the midpoint of the upper plate. At later time (Fig. 6(e), $t = 25$ min), the original split region moves further backwards and the rotation of the clockwise eddy in the corner becomes weaker.

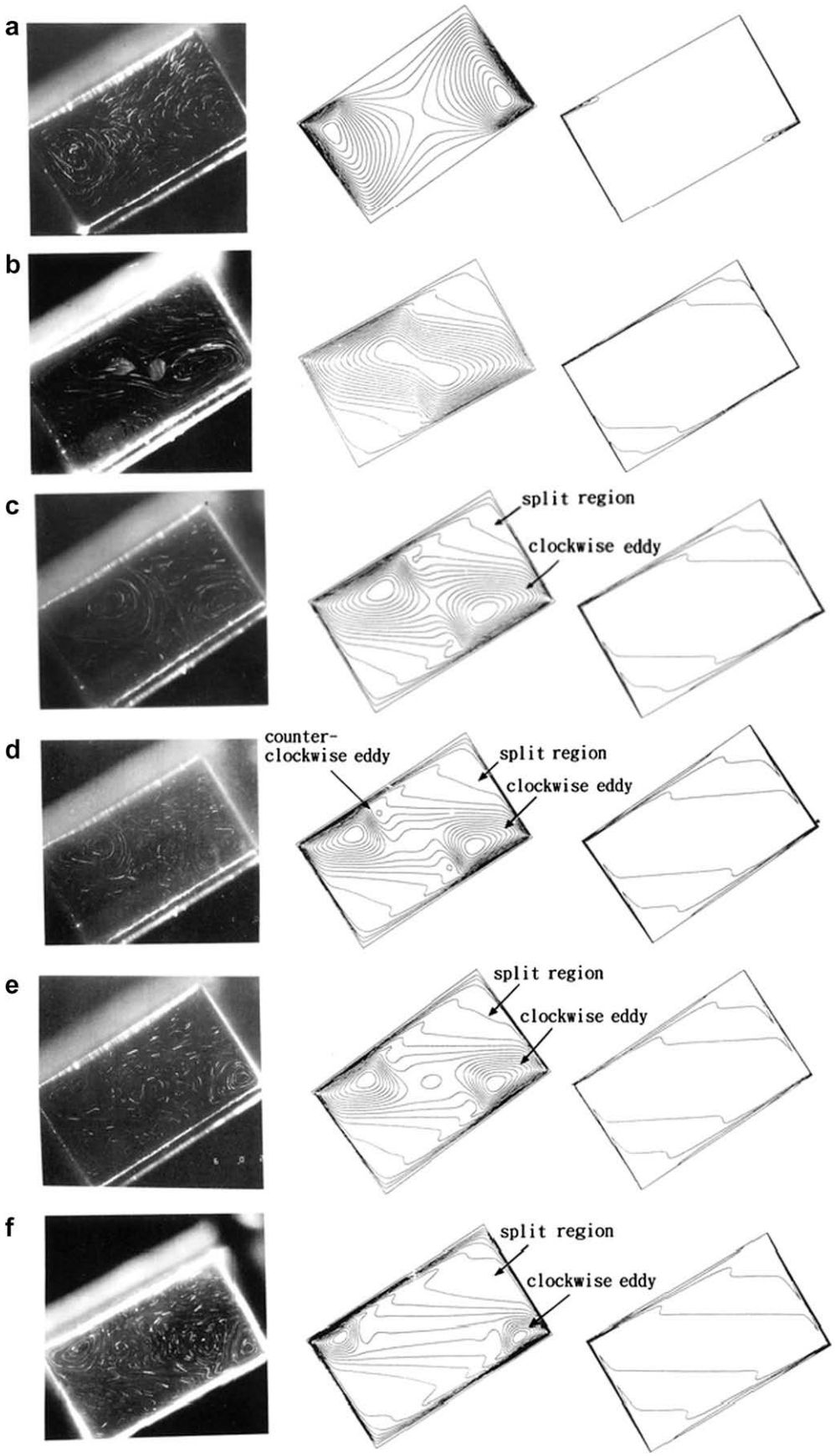

Fig. 6. Comparison of flow structure between experimental observation and prediction for $Ar = 0.6$, $\phi = 60^\circ$ at (a) $t = 1.5$ min, (b) $t = 6$ min, (c) $t = 10$ min, (d) $t = 16$ min, (e) $t = 25$ min, (f) $t = 40$ min and (g) t = 80 min.

4.3. $\phi = 30°$, Ar = 0.6

The flow evolving with time for $\phi = 30°$, $Ar = 0.6$ is shown in Fig. 7(a–c). Initially, two clockwise cells are generated in the bottom-left and top-right hand corners of the enclosure, but quickly merge into a single clockwise cell at $t = 2$ min; a result in direct contrast to that obtained after the same time period for $\phi = 60°$ and $Ar = 0.6$. Note that at later times (Fig. 7(b) for t = 10 min and Fig. 7(c) for $t = 40$ min), a single clockwise cell dominates the entire flow field and persist thereafter. No split of cell is found. This is due to the fact that the stratified layer formed at both the top and the bottom region is very small. It appears that at a small angle of inclination, the mass flow leaving the stratified layer is almost the same or larger than that entering and formation of the stratified layer is difficult. Note that in Fig. 7(c) ($t = 40$ min), the intrusion flow has also diverged also into two streams, once a small stratified region occurs as shown in the prediction of the streamline and iso-concentration line, the split region and turn around phenomena are similar to those observed for $\phi = 60°$. An examination of the constant concentration diagram in Fig. 7(c) reveals that after the intrusion flow in the concentration stratified region arrives at the anode, a portion is forced to turn around. The stream-line diagram indicates that this results in a new split region being generated. This process is very similar to the generation of the internal wave in the flow structure mentioned by Schladow et al. [4]. Therefore, the internal wave motion is also expected to occur for $\phi = 90°$.

Comparing the experimental and numerical results, one finds that initially (Fig. 7(a)), the flow fields match one another, and that an elliptically shaped cell forms in the core with its axis parallel to the insulated wall. At later time for $t = 10$ min and $t = 40$ min, the shape of the circulation cell from the prediction is slightly different from that of the experimental results. Despite of this small discrepancy, both prediction and experiments indicate appearance of a small stratified region in both the top and bottom region.

By using shadowgraph method, one can find that the solutal boundary layer flow is not stable and may protrude into the core like a plume. The solutal plume generated is so narrow and thin which is also called the salt finger. The solutal plume generated randomly along both the electrode surfaces, which persists initially in a short distance along the wall and then protrudes into the core. It appears that the random protrusion and the horizontal motion of the solutal plume along the wall can increase the momentum and

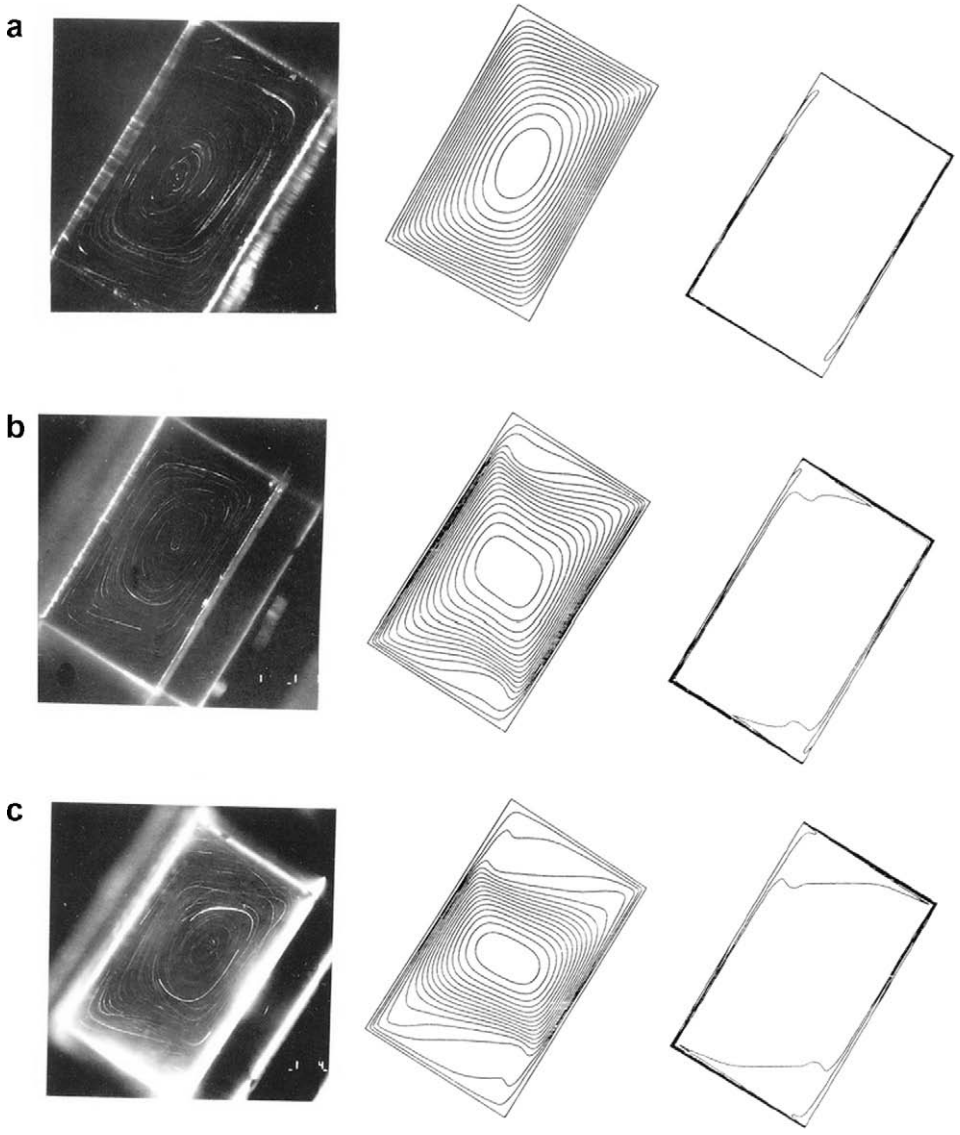

Fig. 7. Comparison of flow structure between experimental observation and prediction of the streamlines and concentration contours for $Ar = 0.6$, $\phi = 30°$ at (a) $t = 2$ min, (b) $t = 10$ min and (c) $t = 40$ min.

species exchange between the boundary layer and the core, and enhance the mass transfer. However, separation of solutal plume from the boundary layer flow can reduce the intrusion flow that enters and forms the stratified layers. Therefore, the occurrence of solutal plume can reduce the growth rate of the stratified layer. When the solutal plume activity become intense for small inclination angle, formation of the stratified layer is not possible. Since in the numerical calculation, the solutal plume activity could not be accounted for, this contributed mostly to the discrepancy between the prediction and the experimental results. At large angle of inclination ($\phi = 60°$), however, the stratification and accumulation of solutal boundary layer flow occurs which makes a clear interface connecting with the core. The occurrence of the stratified layer can make the unitary cell in the core to shrink and to split into double cells at later time. Therefore, a reduction in mass transfer from the anode to the cathode is expected.

For a sufficiently long time, significant difference between the prediction and the experimental result occurs due to that the numerical calculation does not account for generation of solutal plume. In the numerical calculation, the two stratified layers in both the top and the bottom region can be produced which grow with time and eventually combine together to cause an entire stratification of the core. However, in the experiments, the formation of the stratified layer could not occur due to the plume activity, the unitary circulation cell in the core maintains its original structure until when steady state is reached.

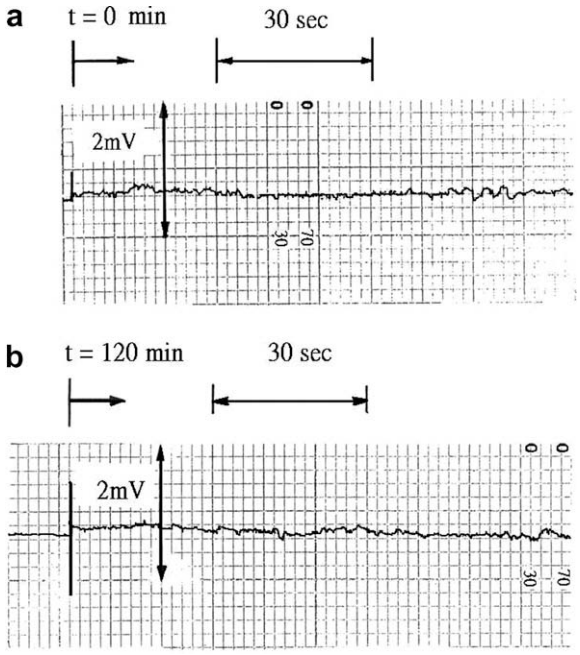

Fig. 8. Concentration fluctuations for $\phi = 90°$ and $Ar = 1$ at (a) $\bar{x} = 0.05$, $\bar{y} = 0.95$ and (b) $\bar{x} = 0.5$, $\bar{y} = 0.95$.

4.4. Concentration oscillations

Although the high-frequency temperature oscillation turns up in both the experimental and theoretical work [2,4,5], the mechanism causing the oscillation is explained in different manners. While Ivey [2] attributes high-frequency oscillation to the internal hydraulic jump, Patterson and Armfield [5] believe it is due to boundary layer instability, since their work was carried out on systems with Fr numbers less than unity where internal hydraulic jump is not expected to occur. Note that the high-frequency temperature oscillations obtained from both of Ivey [2] as well as Patterson and Armfield [5] belong to the same flow regime IV, but they appear in different characteristics. It appears that these different types of high frequency oscillation are due to different mechanisms causing the oscillation. In addition, one could not conclude from their work that flow in other regimes would exhibit such high frequency oscillation phenomena.

In the current experiments, the concentration oscillation measurements are performed, and the exact locations selected for measurements are: 1(0.05, 0.05), 2(0.05, 0.5), 3(0.05, 0.95), 4(0.5, 0.95), 5(0.15, 0.5) and 6(0.5, 0.5) with coordinate system shown in Fig. 2. The results selected for presentation are at point 2(0.05, 0.5) and 3(0.05, 0.95). Point 2 is located at half of the electrode height, which corresponds to the measurement location of temperature at point 1 in the thermal experiments [5]. However, their experiment is performed in flow regime IV where both oscillation of temperature and internal wave of flow are found. The high frequency of temperature fluctuation was initiated, firstly when the start-up intrusion flow accompanying with an unstable traveling wave passes through the thermocouple leads, and secondly when the start up intrusion flow from the heated wall reaches and strikes the opposite cooled wall causing a traveling wave instability along the cooled boundary layer flow. In the current system for $Ar = 1$ and $\phi = 90°$, either low or high frequency oscillation of concentration does not occur, as shown in Fig. 8. The small amplitude fluctuation of concentration is due to the small noise generated in the optical system. It appears that in flow regime III where no internal wave is expected to occur, the traveling wave instabilities on the vertical-wall boundary layers and horizontal intrusion causing the fluctuation in temperature or concentration oscillation does not occur either.

For the case with $\phi = 30°$, concentration oscillation for point 2 starts to occur and becomes intense at later time, as shown in Fig. 9(a). The amplitude of its oscillation reaches maximum at approximately $t = 50$ s and then decreases gradually and becomes

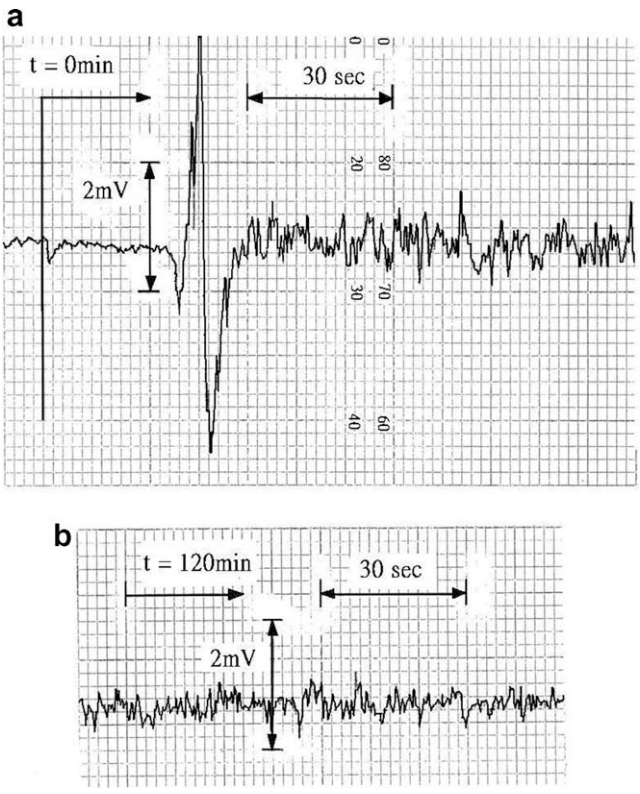

Fig. 9. Concentration fluctuations for $\phi = 30°$, $Ar = 1$ at $\bar{x} = 0.05$, $\bar{y} = 0.95$: (a) in the initial period and (b) at the later time.

steady thereafter at approximately $t = 70$ s. Fig. 9(b) indicates the concentration oscillation at 2 h after initiation of the electrolysis. Both the amplitude and frequency of the concentration oscillation remain approximately the same as at $t = 70$ s.

It appears that the current concentration oscillation is so intense that its occurrence is completely due to the intensive generation of solutal plume. The traveling wave instabilities on the vertical boundary layers and intrusion flow could not be concluded from the current measurements. The initial large amplitude oscillation from $t = 30$ to 70 s is caused by the instability of solutal plume, which deserves a more detailed study. Fig. 10 presents the similar kind of concentration oscillation except that the amplitude is smaller. This is due to the fact that the plume activity in the corner region is much less. Relatively large amplitude oscillation occurs at approximately $t = 25$ s which is earlier than point 2. However, point 3 is at the downstream of point 2. This further suggests that the large amplitude oscillation of concentration is not caused by the traveling wave instability on the vertical boundary layers as found in flow regime IV in a side-heated enclosure [5].

To confirm that the concentration oscillation is caused mainly by the solutal plume, but not any other mechanism; a numerical calculation is performed which does not account for the solutal plume activity. The prediction indicates no oscillation in concentration at any point.

4.5. Mass transfer oscillation

The flow structure observed for $\phi = 30°$ and 60° suggests the occurrence of internal wave motion. Since the oscillation of the entire flow in a side-heated enclosure causes the oscillation of the total heat transfer, PI [2] express numerically the occurrence of internal wave motion in terms of oscillation of the heat transfer Nusselt number in the centerline of the enclosure. Therefore, the same method can be adopted to calculate the oscillation of mass transfer Sherwood number in the centerline of the enclosure. The mathematical equation is written as follows:

$$Sh = \frac{1}{2A}\int_0^1 \left(\bar{u}\times\overline{C} - \frac{\partial\overline{C}}{\partial\bar{x}}\right)_{\bar{x}} \mathrm{d}\bar{y} \tag{5}$$

When $\bar{x} = 0$, Eq. (5) is actually the Sherwood number on the anode. The results of calculation are presented in Fig. 11. For $\phi = 30°$ and $Ar = 0.6$, a periodic oscillation of Sherwood number occur, as shown in Fig. 11(a), with relatively large amplitude at the first cycle and a sharp reduction of amplitude at later cycles. The oscillation of mass transfer from the anode to the cathode clearly demonstrates the occurrence of internal wave motion in the enclosure. This has indicated that the inclination of enclosure can make the internal wave motion to occur. This is due to the fact that at small angle of inclination, the intrusion flow along both the insulated walls can be accelerated, and the impingement of the intrusion flow to the anode or the cathode causes the oscillation of the entire flow. For $\phi = 60°$ and $Ar = 0.6$, the periodic oscillation occurs only for the first cycle, as shown in Fig. 11(b), and decays thereafter. It appears that the acceleration of the intrusion flow is not so effective to cause the internal wave motion when the inclination angle becomes large. For $\phi = 90°$ and $Ar = 0.6$, however, no oscillation of Sherwood number is found [24]. This result agrees with the conclusion of PI that natural convection in flow regime III for $\phi = 90°$ has no internal wave motion. Finally, the effect of aspect ratio on the oscillation of Sherwood number is also studied [24]. The prediction indicates that the effect of Ar on the entire flow oscillation is not significant.

5. Conclusions

In the experiments, the transient natural convection in the vertical enclosure is very complex, such as the secondary cells occurred on the side can induce the counter clockwise vortex in the two corners which leads to the generation of counter clockwise circulation of core as well as the wave-like flow structure at later time. The variation of the inclination and the aspect ratio of the enclosure can change the entire flow structure significantly. When the inclination angle is large, the solutal boundary layer flows can accumulate along both the upper and the lower region of the

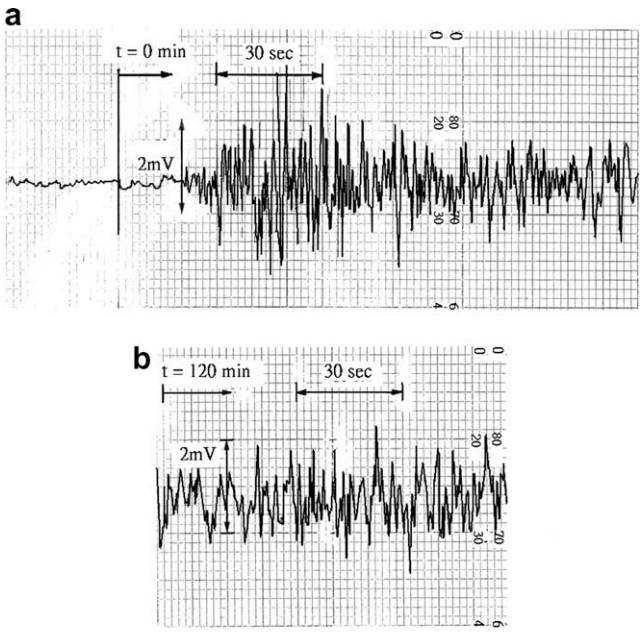

Fig. 10. Concentration fluctuations for $\phi = 30°$, $Ar = 1$ at $\bar{x} = 0.5$, $\bar{y} = 0.95$: (a) in the initial period and (b) at the later time.

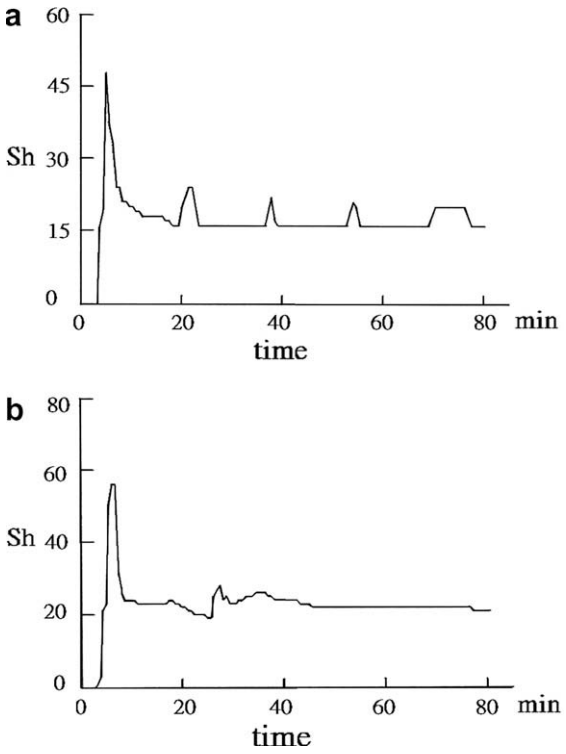

Fig. 11. Sherwood number variation with times at the centerline of the enclosure for (a) $\phi = 30°$, $Ar = 0.6$ and (b) $\phi = 60°$, $Ar = 0.6$.

enclosure and result in a formation and growth of the concentration stratified region. For a small inclination angle, the solutal boundary layer flow can become unstable and lead to generation of solutal plume which penetrates directly into and mix with the core. The plume activity causes strong oscillations of concentration and makes formation of the stratified layers not possible.

For $\phi = 60^\circ$, the flow structure observed suggests occurrence of internal wave motion. However, the concentration oscillation measurements do not provide a clear indication of entire flow oscillation. Therefore, numerical calculation for Sherwood number variation with time was performed, and the results provide a clear evidence of internal wave motion when $\phi < 60^\circ$.

In the transient development of natural convection process, the majority of the experimental and numerical results were in good agreement except those obtained for a vertical enclosure where a very complicated flow structure was observed. The similar flow structure was also observed in the thermal experiments, which could not be simulated by other numerical schemes. Another exception to these results occurred at an inclined angle of 30°, where the numerically simulated and experimentally obtained results differed significantly at later time. This is due to the fact that the numerical calculations could not account for the solutal plume generation, resulting instead, in erroneous predictions of both a concentration stratified region and boundary layer type flow structure as well as many small eddies in the flow field.

References

[1] J.C. Patterson, J. Imberger, Unsteady natural convection in a rectangular cavity, J. Fluid Mech. 100 (1980) 65–68.

[2] G.N. Ivey, Experiments on transient natural convection in a cavity, J. Fluid Mech. 144 (1984) 389–401.

[3] S. Paolucci, D.R. Chenoweth, Transition to chaos in a differentially heated vertical cavity, J. Fluid Mech. 201 (1990) 379–410.

[4] S.G. Schladow, J.C. Patterson, R.L. Street, Transient flow in a side-heated cavity at high Rayleigh number: a numerical study, J. Fluid Mech. 200 (1989) 121–148.

[5] J.C. Patterson, S.W. Armfield, Transient features of natural convection in a cavity, J. Fluid Mech. 219 (1990) 469–497.

[6] S.G. Schladow, Oscillatory motion in a side-heated cavity, J. Fluid Mech. 213 (1990) 589–610.

[7] T.D. Upton, D.W. Watt, Experimental study of transient natural convection in an inclined rectangular enclosure, Int. J. Heat Mass Tran. 40 (11) (1997) 2679–2690.

[8] A.M.H.J.C. Brooker, T.G. Patterson, W. Schopf, Convective instability in a time dependent buoyancy driven boundary layer, Int. J. Heat Mass Tran. 43 (2000) 297–310.

[9] O. Aydin, Transient natural convection in rectangular enclosures heated from bottom and cooled from above, Int. Commun. Heat Mass Tran. 26 (1) (1999) 135–144.

[10] H. Wang, M.S. Hamed, Flow mode-transition of natural convection in inclined rectangular enclosures subjected to bidirectional temperature gradients, Int. J. Therm. Sci. 45 (8) (2006) 782–795.

[11] M.C. Ece, E.N. Buyuk, Natural-convection flow under a magnetic field in an inclined rectangular enclosure heated and cooled on adjacent walls, Fluid Dyn. Res. 38 (8) (2006) 564–590.

[12] S.M. Aminossadati, B. Ghasemi, The effects of orientation of an inclined enclosure on laminar natural convection, Int. J. Heat Technol. 23 (2) (2005) 43–49.

[13] M. Ouriemi, P. Vasseur, A. Bahloul, Natural convection of a binary fluid in a slightly inclined shallow cavity, Numer. Heat Tran. A-Appl. 48 (6) (2005) 547–565.

[14] M. Ouriemi, P. Vasseur, A. Bahloul, Natural convection of a binary mixture confined in a slightly tall enclosure, Int. Commun. Heat Mass Tran. 32 (6) (2005) 770–778.

[15] C. Cianfrini, M. Corcione, P.P. Dell'Omo, Natural convection in tilted square cavities with differentially heated opposite walls, Int. J. Therm. Sci. 44 (5) (2005) 441–451.

[16] H. Yu, N. Li, R.E. Ecke, Scaling in laminar natural convection in laterially heated cavities: Is turbulence essential in the classical scaling of heat transfer?, Phys Rev. E 76 (2) (2007). art. no. 026303.

[17] R.J. Goldstein, H.D. Chaing, V. Srinivasan, A.S. Fleischer, Local mass transfer measurements in an inclined enclosure at high Rayleigh number, Heat Mass Tran./Waerme – und Stoffuebertragung 41 (11) (2005) 991–998.

[18] R.J. Goldstein, H.D. Chiang, D.L. See, High Rayleigh number convection in horizontal enclosure, J. Fluid Mech. 213 (1990) 111–126.

[19] Y. Kamotani, L.W. Wang, S. Ostrach, H.D. Jiang, Experimental study of natural convection in shallow enclosures with horizontal temperature and concentration gradients, Int. J. Heat Mass Tran. 28 (1985) 165–173.

[20] S.V. Patankar, Numerical Heat Transfer and Fluid Flow, Hemisphere Publishing Co., New York, 1980.

[21] C.R. Wilke, M. Eisenberg, C.W. Tobias, Correlation of limiting current under free convection condition, J. Electrochem. Soc. 100 (1953) 513–523.

[22] S.J. Kline, F.A. McClintock, Describing uncertainty in single-sample experiments, Mech. Eng. Jan. (1953) 3–8.

[23] C. Gau, K.H. Wu, A nonintrusive technique for concentration distribution measurement in enclosure, Exp. Heat Transfer 2 (1989) 215–226.

[24] D.Z. Jeng, Experimental and Numerical Study of Steady State and Transient Natural Convection in Inclined Enclosures, Ph.D. Thesis, National Cheng Kung University, Taiwan, 2002.

[25] G. de Vahl Davis, Natural convection of air in a square cavity a bench mark solution, Int. J. Numer. Meth.Fl. 3 (1983) 249–264.

[26] T.F. Lin, C.C. Huang, T.S. Chang, Transient binary mixture natural convection in square enclosures, Int. J. Heat Mass Tran. 33 (2) (1990) 559–574.

[27] M.G. Worster, A.M. Leitch, Laminar free convection in a confined region, J. Fluid Mech. 156 (1985) 301–329.